Nanoscale

Accepted Manuscript

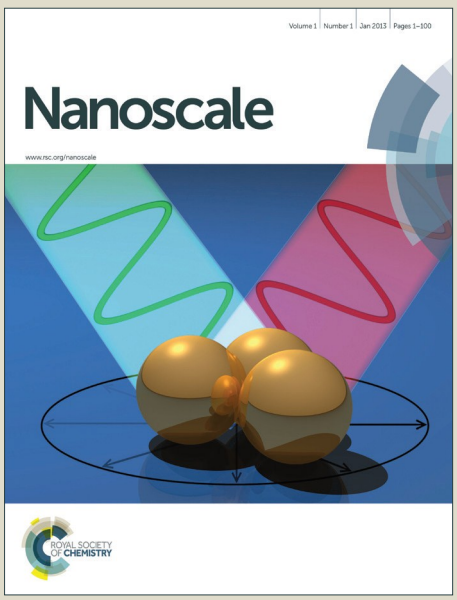

ROYAL SOCIETY OF CHEMISTRY

www.rsc.org/nanoscale

Nanoscale

PAPER

Unexpected Large Capacity of Ultrafine Manganese Oxide as Sodium-Ion Battery Anode

Received 00th January 20xx,
Accepted 00th January 20xx

DOI: 10.1039/x0xx00000x

www.rsc.org/

Yu-Ting Weng,[a] Tzu-Yang Huang,[a] Chek-Hai Lim,[a] Pei-Sian Shao,[a] Sunny Hy,[b] Chao-Yen Kuo,[b] Ju-Hsiang Cheng,[b] Bing-Joe Hwang,[b] Jyh-Fu Lee[c] and Nae-Lih Wu*[a]

MnO_2 is shown for the first time to be electrochemically active as a conversion anode for Na-ion batteries (NIBs). Space-confined ultrafine (UF)-MnO_2, with an average crystal size of 4 nm, synthesized using a porous silicon dioxide templated hydrothermal process exhibits a high reversible sodiation capacity of 567 mAh g^{-1}, in contrast to negligible activity shown by the aggregates of larger (14 nm) MnO_2 nanocrystallites. The remarkably enhanced sodiation activity of the UF-MnO_2 is attributable to the greatly reduced crystal size, which facilitates diffusion of Na ions, along with high surface energy arising from extensive heterogeneous interfacial bonding with the SiO_2 surrounding. The UF-MnO_2 anode exhibits exceptional rate and cycle performance, exhibiting >70% capacity retention after 500 cycles. In operando synchrotron X-ray absorption near-edge structure analysis reveals combined charge–storage mechanisms involving conversion reaction between Mn(III) and Mn(II) oxides, Mn(III)–$O_{1.5}$ + Na^+ + e^- ↔ 1/2 Na_2O + Mn(II)–O, and non-Mn-centered redox reactions. The finding suggests a new strategy for "activating" the potential electrochemical electrode materials that appear inactive in the bulk form.

Introduction

Developing rechargeable batteries is a major preoccupation of electric vehicle and renewable energy storage system manufacturers. In past years, there have been extensive efforts in research and development of lithium (Li)-ion batteries (LIBs) for higher energy density and longer cycle life. However, because of the limited resources of Li and its high cost, problems exist in meeting the demand for large-scale energy storage applications. Consequently, research on using alternative reliable energy storage technologies has increased. Sodium (Na)-ion batteries (NIBs) have recently attracted increasing attention because, compared with Li, Na is widely available and inexpensive. Because NIBs possess an electrochemical nature similar to that of LIBs, there is a growing trend of using LIB electrode materials, such as carbon materials (hard carbon[1–6], graphene[7,8]), alloy materials (tin[9–13], germanium[14,15], antimony[16–20]), metal sulfides (MoS_2[21–23], SnS_2[24], Sb_2S_3[25], WS_2[26], FeS[27]), transition metal oxides and phosphates (SnO[28,29], TiO_2[30–32], CuO[33,34], Fe_2O_3[35,36], Co_3O_4[37], MoO_3[38], $Na_3Ti_2P_2O_{10}F$[39]), and organic materials[40] as anodes in NIBs. Compared with other conversion-type metal oxide anodes in LIBs, manganese oxides (MnO_x) have the advantages of high theoretical capacity, natural abundance, low cost, and environmental benignity. In addition, it shows a smaller potential hysteresis[41] and lower operation potential (1.032 V vs. Li/Li^+)[42]. In spite of various studies of MnO_x as LIB anodes, there has surprisingly been no report on electrochemical activity of MnO_x as NIB anodes, and the reason for different electrochemical activities of MnOx in LIBs and NIBs is unknown.

Undoubtedly, structural parameters, such as size and morphology, of active materials are essential for optimizing the performance of electrochemical electrodes. For LIBs, nanostructured MnO_x materials have been shown in some cases to deliver superior electrochemical performance than their bulk counterparts because of large surface areas and the shortening of the Li^+ diffusion path, both of which are beneficial to the rate performance.[43–47] Moreover, ultrafine (UF) nanoscale materials possess high surface energies with strong interaction with the surrounding, and this property may provide opportunities for substantially enhancing electrochemical activity. In this work, we developed a new synthesis strategy to realize the formation of spatially confined UF-MnO_2 nanocrystallites that are in average 4 nm in size. When this new nanostructured MnO_2 material was tested as an anode for NIB application, it exhibited an unexpected high electrochemical sodiation capacity, in contrast to negligible activity shown by the aggregates of larger (14 nm) MnO_2 crystallites. This is the first time that MnO_2 is shown to be electrochemically active as a NIB conversion anode.

Experimental section

Synthesis of MnO_2/SiO_2 and MnO_2

Mesoporous SiO_2 nanoparticles were purchased from Sigma-Aldrich, and analytical grade chemical reagents were used. To synthesize MnO_2, 0.5 g of $KMnO_4$ was added to 40 mL of an aqueous dispersion solution containing 1.92 g of SiO_2 and the solution was

[a] Department of Chemical Engineering, National Taiwan University, Taipei 106, Taiwan
[b] Department of Chemical Engineering, National Taiwan University of Science and Technology, Taipei 106, Taiwan
[c] National Synchrotron Radiation Research Center, Hsinchu 30076, Taiwan

heated at 150 °C for 48 h. After washing with distilled water, brownish MnO_2/SiO_2 powder (precipitate) was obtained. The composite precipitate was subsequently etched with a 1 M NaOH solution for 12 h, washed with distilled water, and finally air-dried at 60 °C. In addition, pure MnO_2 was synthesized under the same hydrothermal condition without the presence of SiO_2, and the obtained powder was not subjected to etching.

Material characterization

Microstructural characterization was performed using scanning electron microscopy (SEM; JSM-7600F, JEOL) and transmission electron microscopy (TEM; FEI Tecnai TF20, Philips). Pore size distribution was determined using Barrett-Joyner-Halenda (BJH) analysis of N_2 adsorption (Micromeritics ASAP 2020). Powder X-ray diffraction (XRD) was performed using a diffractometer (X-pert/Philips) with Cu K_α radiation. X-ray photoelectron spectroscopy (XPS) analysis was carried out with a spectroscope (VG Scientific/ESCALAB 250) equipped with an Al X-ray source (Kα, 1486.6 eV) operated at 15 kV and 100 W. In operando X-ray absorption near-edge spectroscopy (XANES) analysis was conducted using 17-C1 beamline of the National Synchrotron Radiation Research Center in Taiwan. Spectra were acquired during the course of a constant-current discharge cycle with a current density between 2.8 and 0 V. The collected data were further analyzed using the IFEFFIT program.

Electrochemical measurements

The working electrodes were prepared by mixing 75 wt.% active materials (MnO_2/SiO_2 nanocomposite or pure MnO_2), 15 wt.% conductive additive (multiwall carbon nanotube), and 10 wt.% binder (alginate) to form a homogenous slurry, which was then coated on a copper foil, followed by drying at 100 °C for 12 h in a vacuum oven. To test electrochemical properties, 2032-type coin cells were assembled in an argon-filled glove box with Na foil as the counter and reference electrode. The electrolyte was 1.0 M sodium hexafluorophosphate ($NaPF_6$) in a mixture solvent of ethylene carbonate (EC) and propylene carbonate (PC) (EC: PC= 1:1, v/v), and the separator was a glass microfiber filter (Whatman). Galvanostatic charge–discharge tests were performed with a cut-off voltage range of 0.001–2.8 V (vs. Na^+/Na) by using the MCN6410 Arbin battery testing system. Specific capacity was expressed based on the mass of MnO_2.

Results and discussion

Material characterizations

MnO_2 is known to be susceptible to sintering and hence easily grows into large crystal sizes upon thermal treatment. In order to limit the dimension growth of the MnO_2 nanocrystallites, a new synthesis method using mesoporous SiO_2 particles as a solid template was developed. Nanocrystalline MnO_2 was deposited within the pores of the SiO_2 template via a hydrothermal process. As shown by SEM analysis, the SiO_2 particles had a spherical shape and a granular surface (Fig. 1a; Fig. S1a for low magnification), and as revealed by TEM analysis, they were mesoporous and contained regular arrays of pores (Fig. 1b). The MnO_2/SiO_2 composite particles obtained from the hydrothermal treatment exhibited smooth solid surfaces (Fig. 1c) and were opaque under TEM (Fig. 1d). MnO_2 appeared to preferentially deposit within the SiO_2 particles, and only a small amount of MnO_2 flakes was observed attached to the composite particle surfaces. Subsequent treatment of the composite particles with an alkaline aqueous solution to remove the SiO_2 led to the formation of different hollow interior structures (Fig. 2a–d; Fig. S1b for low magnification). Energy-dispersive X-ray (EDX) analysis indicated that the remaining skeletons of the hollow spheres contained both Si and Mn. Line-scan analysis (Fig. 2d) showed intimate coexistence between these two elements within the resolved scale. SiO_2 that remained in the skeleton after prolonged etching apparently had chemical properties different from those of pure SiO_2, which would have completely dissolved in the alkaline solution. The brownish color of the MnO_2/SiO_2 composite suggests doping of SiO_2 by Mn ions, and the doping may have reduced the solubility of SiO_2 in the alkaline solution. High-resolution TEM analysis revealed a domain structure within the remaining skeleton (Fig. 2e, f).

N_2 adsorption analysis further indicated that the SiO_2 template particles had a narrow pore size distribution between 2.0 and 4.5 nm (Fig. 3) and a pore volume of 0.94 $cm^3\ g^{-1}$. MnO_2 deposition resulted in remarkable reduction in the pore volume, indicating that MnO_2 successfully occupied pores within the SiO_2 matrix. The etched MnO_2/SiO_2 nanocomposite powder also showed the absence of meso- and micropores (Fig. 3); therefore, the etched powder was a macroporous material with a solid skeleton that contained numerous UF-MnO_2 nanodomains. It was found that Mn could not completely be leached out by the conventional nitric acid digestion treatment; the Mn content determined from the inductively coupled plasma analysis was always lower than those determined from the EDX analysis. Extensive EDX analysis indicated a Mn content, in terms of

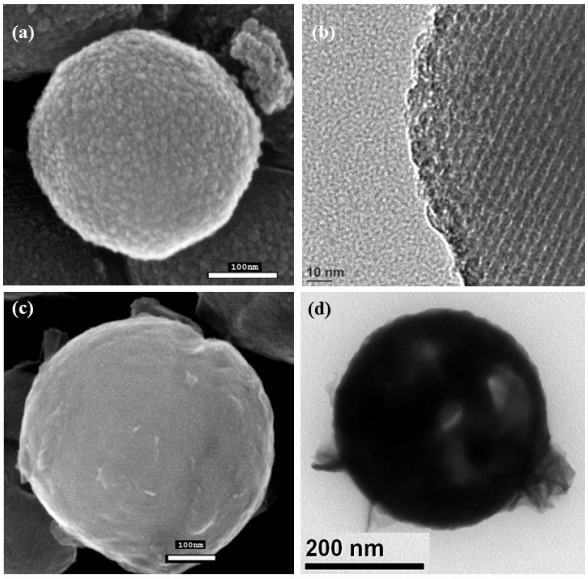

Fig. 1 (a) SEM and (b) TEM micrographs of fresh SiO_2 template particles and (c) SEM and (d) TEM micrographs of the SiO_2 particles after the hydrothermal deposition of MnO_2.

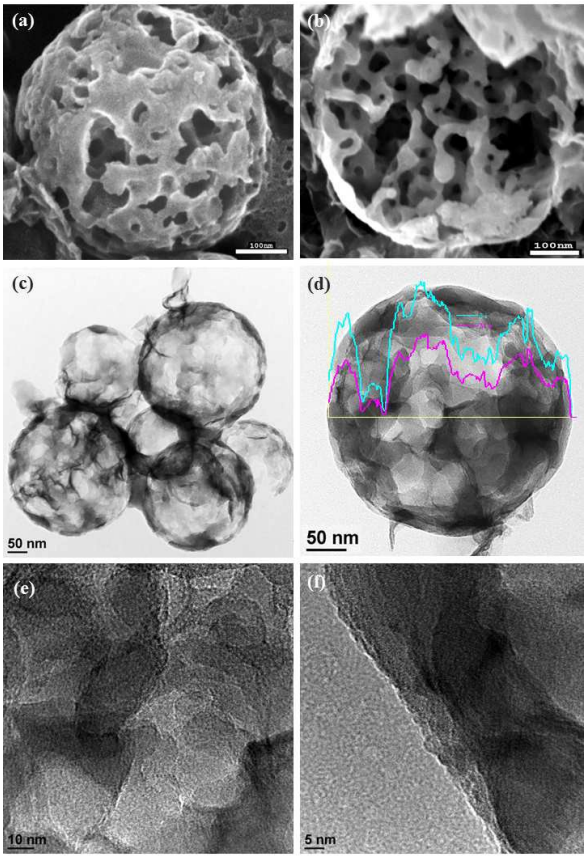

Fig. 2 (a,b) SEM and (c,d) TEM micrographs showing the hollow interior of the MnO_2/SiO_2 composite particles after etching with an alkaline solution for 12 h and (e,f) high-resolution TEM of the remaining solid skeleton of the etched MnO_2/SiO_2 composite particles.

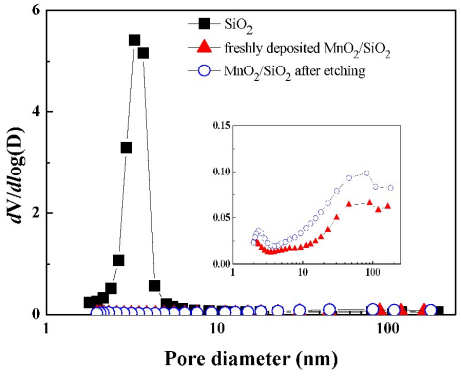

Fig. 3 Nitrogen adsorption pore distributions of (■) SiO_2 powder; (▲) freshly deposited MnO_2/SiO_2; and (○) MnO_2/SiO_2 after etching with an alkaline solution. The inset shows enlarged plots of the MnO_2/SiO_2 samples.

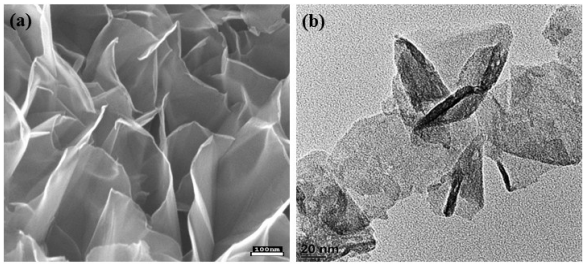

Fig. 4 (a) SEM and (b) TEM micrographs of the MnO_2 control powder.

MnO_2, of 32% (±3%) by weight. The control MnO_2 powder had a flake-like morphology with widths extending up to a few hundred nanometers (Fig. 4).

XRD analysis of the porous MnO_2/SiO_2 nanocomposite showed reflections of MnO_2–birnessite and a broad hump near 2θ = ~22° attributable to the amorphous SiO_2 component (Fig. 5). By contrast, the MnO_2 control powder showed reflections of only birnessite. The reflection peaks of birnessite from the MnO_2/SiO_2 nanocomposite were much broader than those of the MnO_2 control powder, suggesting that the average size of the birnessite crystallites in the MnO_2/SiO_2 composite was much smaller than that in the MnO_2 control powder. We estimated the crystallite size by using the Debye–Scherrer equation[48] and obtained an average birnessite crystallite size of 4.2 nm for MnO_2 in the MnO_2/SiO_2 nanocomposite and of 13.8 nm in the MnO_2 control powder. The size of the birnessite crystallite in the composite closely matched the pore dimensions of the starting SiO_2 powder. This consistency in dimensions further proved that the birnessite crystallites mainly formed within the pores of the SiO_2 matrix. For the MnO_2 control powder, the XRD-determined birnessite crystallite size was much smaller than the flake dimensions shown by the microscopic analysis (Fig. 4). Therefore, we conclude that the MnO_2 flakes were polycrystalline and they were aggregates of birnessite nanocrystallites.

For XPS analysis (Fig. 6), the Mn $2p_{3/2}$ spectrum of the MnO_2 control powder was typical of birnessite, showing a strong Mn(IV) contribution that appeared as a characteristic multiplet with a maximum at 642.2 eV, and two satellite peaks at higher binding energies of 643.2 and 644 eV[49], along with a small contribution of Mn(III) at 640.7 eV. The spectrum of the composite powder was substantially broader (by 1.9 eV at half-maximum) than that of the control MnO_2, and it showed a red-shift, by 0.5 eV, of the Mn^{4+} maximum peak to 641.7 eV with the multiplet intensity ratios departed from those of the control powder. These differences were attributable to the variations in the bonding environment of Mn(IV) ions in the composite sample associated with the Mn−O−Si bonding at the interfaces between the SiO_2 and MnO_2 domains as well as within the doped SiO_2. This was consistent with a reported lower binding energy of Mn(IV) ions in $MnSiO_4$ than in MnO_2[50], presumably due to reduced ionic nature of the Mn−O−Si bonding. As revealed in various geological settings[51], the formation of Mn–O–Si oxides is facile under hydrothermal conditions. Through the formation of Mn–O–Si bonding, the SiO_2 surfaces may act as

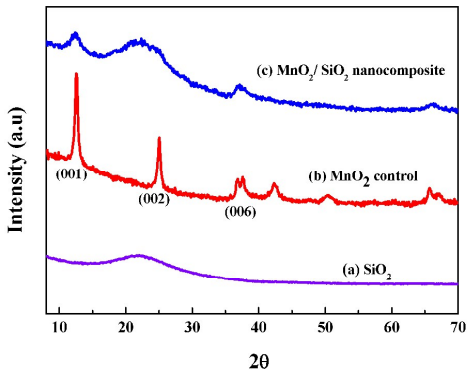

Fig. 5 XRD patterns of (a) SiO_2 template powder, (b) MnO_2 control powder, and (c) etched MnO_2/SiO_2 powder. The (*hkl*) indices belong to birnessite.

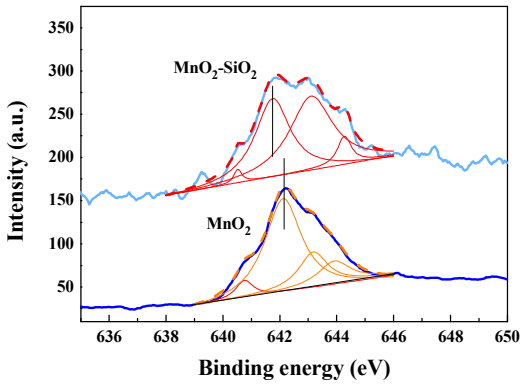

Fig. 6 Mn2$p_{3/2}$ XPS spectra of the MnO_2/SiO_2 composite and MnO_2 control powders.

favorable heterogeneous nucleation sites for MnO_2 formation during hydrothermal synthesis, leading to the preferential deposition of UF−MnO_2 crystallites within the SiO_2 matrix with high surface energy arising from extensive heterogeneous interfacial bonding.

Electrochemical performance of MnO_2 powders as NIB anodes

The electrochemical performance of MnO_2 powders with different crystal sizes as NIB anodes was investigated and the results are shown in Fig. 7. Control study indicated that pure SiO_2 did not show reversible capacity. The pristine MnO_2 control powder exhibited a reversible charge capacity of only 19 mAh g^{-1}. The MnO_2 control powders with or without being subjected to the etching process exhibited the same low sodiation activity. The small charge capacity exhibited by the MnO_2 control electrode explains why there has so far been no report of MnO_x as NIB anode. In great contrast, the first discharge of the UF−MnO_2 electrode showed a plateau between 0.8 and 0.6 V, which signified extensive reduction of MnO_2, followed by a tail, giving a total sodiation capacity of nearly 1000 mAh g^{-1}. The first charge of the UF−MnO_2 anode showed a sloped plot giving the first cycle reversible capacity of 567 mAh g^{-1}. The large irreversible capacity during the first cycle may be attributable to the combination of SEI formation and, as shown later, irreversible reduction of the starting MnO_2 to the oxides of lower Mn valences. The remarkable crystal-size effect within the nanometer range observed on the electrochemical sodiation activity of MnO_2 is unique among other metal oxide-based NIB anodes. The voltage plots of the second cycle exhibited sloped profiles, lacking distinct plateau. Sloped charge/discharge voltage profiles are typically seen on various conversion oxide NIB anodes.[35−39]

Fig. 7b and c respectively summarize the specific capacity data and charge–discharge voltage plots at different current densities. The Coulombic efficiency quickly increased to >95% after 5 cycles. The UF-MnO_2 anode retained a specific capacity of 130 mAh g^{-1} when the current rate was increased by 100-fold to 3750 mA g^{-1}. When cycled at 150 mA g^{-1}, the UF−MnO_2 anode retained nearly 70% of the initial capacity after 500 cycles (Fig. 7d), indicating exceptional cycle performance. Table 1 compares the specific capacity of the UF−MnO_2 electrode with those of various NIB conversion anodes that have been prepared by the similar slurry coating process in previous studies. As shown, the UF−MnO_2 exhibited higher specific capacity than those of the other oxides and superior cycle performance. The data illustrate the promising potential for the low-cost MnO_2–based NIB conversion anode. The finding of the present work suggests a new strategy for "activating" the potential

Table 1 Comparison in electrochemical performance of NIB conversion anodes

Oxide	Morphology	First cycle reversible specific capacity (mAh g^{-1})	Capacity retention/ cycle number	Ref. no.
UF-MnO_2	4 nm crystallites confined by SiO_2	567	70%/500	this study
CuO	Nanowire	480	63%/50	35
Fe_2O_3	2 nm crystallites @Graphene	410	98%/200	36
Fe_2O_3	5 nm crystallites	400	71%/60	37
Co_3O_4	nano crystallites	450	N.A.	38
MoO_3	nano crystallites	250	65%/10	39
MoS_2	nanosheet	190	79%/100	23

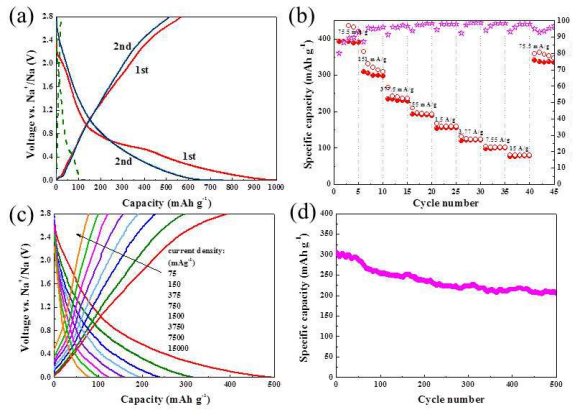

Fig. 7 Electrochemical characterizations: (a) the first and second cycle charge–discharge voltage plots of the UF-MnO_2 electrode (solid lines) and the first cycle plots of the MnO_2 control electrode (dashed line) acquired at 37.5 mAh g^{-1}; (b) specific capacity and Coulombic efficiency of the UF-MnO_2 electrode for different current densities; (c) charge–discharge voltage plots of the UF-MnO_2 electrode at different current densities; and (d) specific capacity versus cycle number of the UF-MnO_2 electrode at a current density of 150 mA g^{-1}.

electrochemical electrode materials that appear inactive in the bulk form.

Ex-situ XRD study on electrodes discharged to potentials below 1.0 V did not detect any crystalline refection, indicating that birnessite turned into amorphous phases upon the first sodiation cycle (Figure S2). The charge storage mechanism was investigated using in operando synchrotron XANES analysis during the course of the second discharge (inset, Fig. 8a). Fig. 8 shows the selected six spectra acquired consecutively with equal capacity increment. At the beginning of discharge (2.5 V), the XANES spectrum was located between the standard spectra of MnO and Mn_2O_3 standard spectra, indicating an average Mn valence between 2+ and 3+ (Fig. 8a). With decreasing potential, the XANES spectrum shifted toward lower energy with the profile evolving more closely to that of MnO (Fig. 8a), until the potential reached approximately 0.35 V. Isosbestic points (i.e., common intersection points) that matched closely to those of crystalline Mn_2O_3 and MnO were found (Fig. 8a), suggesting a two-phase conversion reaction involving a reduction reaction between Mn(III) and Mn(III) oxides:

$$Mn(III)–O_{1.5} + Na^+ + e^- \leftrightarrow 1/2\ Na_2O + Mn(II)–O$$

where Mn(III)–$O_{1.5}$ and Mn(II)–O represent local chemical stoichiometries of MnOx domains, but do not necessarily correspond to the crystalline MnO or Mn_2O_3 structure.

Below 0.35 V, the spectrum essentially remained unchanged (Fig. 8b), indicating that the charge-storage below this potential originated primarily from mechanisms that do not involve Mn ions. Non-metal-centered redox reactions, such as the formation of polymer-like film and surface space-charge layer[52–53], at low potentials have been

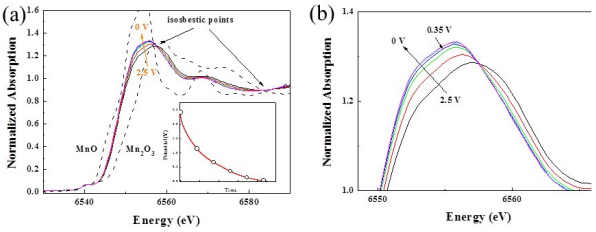

Fig. 8 In operando synchrotron XANES spectra acquired during the second discharge (inset) of the UF-MnO_2 electrode.

suggested to make substantial contribution to capacity of the conversion anodes in LIBs. We infer that similar non-Mn-centered redox reactions also occur in the present system, and they account for majority of the storage capacity taking place below 0.35 V.

Until the end of discharge, there was no formation of metallic Mn. This is in contrast to what have been reported for other NIB conversion anodes as well as the MnO_x anodes of LIBs, which are completely reduced to zero-valence metal during the first lithiation and undergo reversible redox reactions between the metal and oxides [54-56]:

$$MO_x + 2x\ Li^+ (or\ Na^+) + 2x\ e^- \leftrightarrow x\ Li_2O + M.$$

The inability to reduce the Mn oxide into Mn metal during the discharge process suggests significant polarization built up within the oxide crystallites upon sodiation. The polarization may arise from diffusion resistance of Na ion within the oxide crystallite or high activation energy of the conversion reaction. Na ion is substantially larger than Li ion, and therefore diffusion of Na ions within the oxide crystallite is expected to encounter a much greater resistance than Li ions. Reducing the crystal size can shorten the diffusion path of the Na ions and hence decrease the polarization. The reduction potential to metallic Mn is substantially lower, by 0.7~1.3 V[57], than those to the other metals in the oxides listed in Table 1. This may explain why MnO_2 conversion anode is more size-sensitive than the other oxide conversion anodes. Furthermore, we cannot rule out the possibility that the high surface energy of the UF-MnO_2 crystallites arising from extensive heterogeneous interfacial bonding with the SiO_2 surrounding helps to lower the activation energy for initiating the conversion reaction and hence facilitates the sodiation process.

Conclusions

Space-confined UF-MnO_2 with an average crystal size of approximately 4 nm was synthesized through a SiO_2-templated hydrothermal process. UF-MnO_2 exhibited a reversible sodiation capacity of 567 mAh g^{-1}, compared with the negligible activity shown by aggregates of larger (14 nm) MnO_2 crystallites. Our results indicated a profound size effect within the nanometer range that was previously unknown among other conversion-reaction NIB anodes. The UF-MnO_2 anode exhibited exceptional rate and cycle performance, exhibiting >70% capacity retention after 500 cycles at 0.15 A

g^{-1}. The enhanced cycle stability may be attributable to the solid-embedding architecture that enabled the reduction in the dimensional variations of the active material. In operando XANES analysis revealed combined charge–storage mechanisms involving conversion reaction between Mn(III) and Mn(II) oxides and non-Mn-centered redox reactions that dominated at low potentials.

Acknowledgements

This work was financially supported by the Ministry of Science and Technology (MOST), Taiwan (NSC 101-2221-E-002-160-MY3 and MOST 104-ET-E-002-001-ET). Y. T. W. thanks MOST for the postdoctoral fellowship (MOST 103-2811-E-002-003, 104-2811-E-002-005). C. H. L. thanks National Taiwan University (NTU) for the postdoctoral fellowship (NTU 103R4000). The authors thank S.J. Ji of MOST (National Taiwan University) for helping in the SEM analysis.

Notes and references

1 H. Song, N. Li, H. Cui and C. Wang, *Nano Energy,* 2014, **4**, 81.
2 J. Ding, H. Wang, Z. Li, A. Kohandehghan, K. Cui, Z. Xu, B. Zahiri, X. Tan, E. M. Lotfabad, B. C. Olsen and D. Mitlin, *ACS nano*, 2013, **7**, 11004.
3 J. Zhao, L. Zhao, K. Chihara, S. Okada, J. Yamaki, S. Matsumoto, S. Kuze and K. Nakane, *J. Power Sources*, 2013, **244**, 752.
4 K. Tang, L. Fu, R. J. White, L. Yu, M. M. Titirici, M. Antonietti and J. Maier, *Adv. Energy Mater*., 2012, **2**, 873.
5 Y. Cao, L. Xiao, M. L. Sushko, W. Wang, B. Schwenzer, J. Xiao, Z. Nie, L. V. Saraf, Z. Yang and J. Liu, *Nano Lett*., 2012, **12**, 3783.
6 S. Komaba, W. Murata, T. Ishikawa, N. Yabuuchi, T. Ozeki, T. Nakayama, A. Ogata, K. Gotoh and K. Fujiwar, *Adv. Funct. Mater*., 2011, **21**, 3859.
7 Y. Yan, Y. X. Yin, Y. G. Guo and L. J. Wan, *Adv. Energy Mater*., 2014, **4**, 1301584 1.
8 Y. X. Wang, S. L. Chou, H. K. Liu and S. X. Dou, *Carbon*, 2013, **57**, 202.
9 X. Han, Y. Liu, Z. Jia, Y. C. Chen, J. Wan, N. Weadock, K. J. Gaskell, T. Li and L. Hu, *Nano Lett*., 2014, **14**, 139.
10 H. Zhu, Z. Jia, Y. Chen, N. Weadock, J. Wan, O. Vaaland, X. Han, T. Li and L. Hu, *Nano Lett*., 2013, **13**, 3093.
11 Y. Xu, Y. Zhu, Y. Liu and C. Wang, *Adv. Energy Mater*., 2013, **3**, 128.
12 Y. Liu, Y. Xu, Y. Zhu, J. N. Culver, C. A. Lundgren, K. Xu and C. Wang, *ACS nano*, 2013, **7**, 3627.
13 M. K. Datta, R. Epur, P. Saha, K. Kadakia, S. K. Park and P. N. Kumt, *J. Power Sources*, 2013, **225**, 316.
14 L. Baggetto, J. K. Keum, J. F. Browning and G. M. Veith, *Electrochem. Commun*., 2013, **34**, 41.
15 P. R. Abel, Y. M. Lin, T. Souza, C. Y. Chou, A. Gupta, J. B. Goodenough, G. S. Hwang, A. Heller and C. B. Mullins, *J. Phys. Chem. C*, 2013, **117**, 18885.
16 L. Ji, M. Gu, Y. Shao, X. Li, M. H. Engelhard, B. W. Arey, W. Wang, Z. Nie, J. Xiao, C. Wang, J. G. Zhang and J. Liu, *Adv. Mater*., 2014, **26**, 2901.
17 L. Wu, X. Hu, J. Qian, F. Pei, F. Wu, R. Mao, X. Ai, H. Yang and Y. Cao, *Energy Environ. Sci*., 2014, **7**, 323.
18 B. Farbod, K. Cui, W. P. Kalisvaart, M. Kupsta, B. Zahiri, A. Kohandehghan, E. M. Lotfabad, Z. Li, E. J. Luber and D. Mitlin, *ACS nano*, 2014, **8**, 4415.
19 Y. Zhu, X. Han, Y. Xu, Y. Liu, S. Zheng, K. Xu, L. Hu and C. Wang, *ACS nano*, 2013, **7**, 6378.
20 A. Darwiche, C. Marino, M. T. Sougrati, B. Fraisse, L. Stievano and L. Monconduit, *J. Am. Chem. Soc*., 2012, **134**, 20805.
21 L. David, R. Bhandavat and G. Singh, *ACS nano*, 2014, **8**, 1759.
22 C. Zhu, X. Mu, P. A. van Aken, Y. Yu and J. Maier, *Angew. Chem*., 2014, **126**, 2184.
23 G. S. Bang, K. W. Nam, J. Y. Kim, J. Shin, J. W. Choi and S. Y. Choi, *ACS Appl. Mater. Interfaces*, 2014, **6**, 7084.
24 X. Xie, D. Su, S. Chen, J. Zhang, S. Dou and G. Wang, *Chem. Asian J*., 2014, **9**, 1611.
25 D. Y. W. Yu, P. V. Prikhodchenko, C. W. Mason, S. K. Batabyal, J. Gun, S. Sladkevich, A. G. Medvedev and O. Lev, *Nat. Commun*., 2013, **4**, 2922 1.
26 D. Su, S. Dou and G. Wang, Chem. Comm., 2014, 50, 4192.
27 Z. Shadike, Y. N. Zhou, F. Ding, L. Sang, K. W. Nam, X. Q. Yang and Z. W. Fu, *J. Power Sources*, 2014, **260**, 72.
28 M. Gu, A. Kushima, Y. Shao, J. G. Zhang, J. Liu, N. D. Browning, J. Li and C. Wang, *Nano Lett*., 2013, **13**, 5203.
29 D. Su, H. J. Ahn and G. Wang, *Chem. Comm*., 2013, **49**, 3131.
30 K. T. Kim, G. Ali, K. Y. Chung, C. S. Yoon, H. Yashiro, Y. K. Sun, J. Lu, K. Amine and S. T. Myung, *Nano Lett*., 2014, **14**, 416.
31 L. Wu, D. Buchholz, D. Bresser, L. G. Chagas and S. Passerini, *J. Power Sources*, 2014, **251**, 379.
32 Y. Xu, E. M. Lotfabad, H. Wang, B. Farbod, Z. Xu, A. Kohandehghan and D. Mitlin, *Chem. Comm*., 2013, **49**, 8973.
33 S. Yuan, X. Huang, D. Ma, H. Wang, F. Meng and X. Zhang, *Adv. Mater*., 2014, **26**, 2273.
34 L. Wang, K. Zhang, Z. Hu, W. Duan, F. Cheng and J. Chen, *Nano Res*., 2014, **7**, 199.
35 Z. Jian, B. Zhao, P. Liu, F. Li, M. Zheng, M. Chen, Y. Shi and H. Zhou, *Chem. Comm*., 2014, **50**, 1215.
36 M. Valvo, F. Lindgren, U. Lafont, F. Björefors and K. Edström, *J. Power Sources*, 2014, **245**, 967.
37 M. M. Rahman, A. M. Glushenkov, T. Ramireddy and Y. Chen, *Chem. Comm*., 2014, **50**, 5057.
38 S. Hariharan, K. Saravanan and P. Balaya, *Electrochem. Commun*., 2013, **31**, 5.
39 Z. Ma, Y. Wang, C. Sun, J. A. Alonso, M. T. Fernández-Díaz and L. Chen, *Sci. Rep.*, 2014, **4**, 7231.
40 H. Wang, P. Hu, J. Yang, G. Gong, L. Guo, X. Chen, *Adv. Mater.*, 2015, **27**, 2348.
41 L. Ji, Z. Lin, M. Alcoutlabi and X. Zhang, *Energy Environ. Sci*., 2011, **4**, 2682.
42 X. Gu, L. Chen, Z. Ju, H. Xu, J. Yang and Y. Qian, *Adv. Funct. Mater*., 2013, **23**, 4049.
43 H. Jiang, Y. Hu, S. Guo, C. Yan, P. S. Lee and C. Li, *ACS nano*, 2014, **8**, 6038.
44 L. Li, A. R. O. Raji and J. M. Tour, *Adv. Mater*., 2013, **25**, 6298.
45 Y. Ma, C. Fang, X. Ding, G. Ji and J. Y. Lee, *Adv. Mater*., 2013, **25**, 4646.
46 Y. Xia, Z. Xiao, X. Dou, H. Huang, X. Lu, R. Yan, Y. Gan, W. Zhu, J. Tu, W. Zhang and X. Tao, *ACS nano*, 2013, **7**, 7083.
47 Y. Sun, X. Hu, W. Luo, F. Xia and Y. Huang, *Adv. Funct. Mater*., 2013, **23**, 2436.
48 F. W. Jones, *Proc. Roy. Soc. Ser. A*, 1938, **166**, 16.
49 X. Liang, C. Hart, Q. Pang, A. Garsuch, T. Weiss and L. F. Nazar, *Nat. Commun*., 2015, **6**, 5682.
50 D. Briggs and M. P. Seah, Eds., "Practical Surface Analysis," vol. 1, John Wiley & Sons, New York, NY, USA, 2nd edition, 1993.

51 Z. Sun, H. Zhou, G. P. Glasby, Q. Yang, X. Yin, J. Li and Z. Chen, *J. Asian Earth Sci*., 2012, **43**, 64.
52 S. Laruelle, S. Grugeon, P. Poizot, M. Dollé, L. Dupont and J. M. Tarascon, *J. Electrochem. Soc*., 2002, **149**, A627.
53 P. Balaya, H. Li, J. Kienle and J. Maier, *Adv. Funct. Mater*., 2003, **13**, 621.
54 K. Zhong, B. Zhang, S. Luo, W. Wen, H. Li, X. Huang, and L. Chen, *J. Power Sources*, 2011, **196**, 6802.
55 R. C. Lee, Y. P. Lin, Y. T. Weng, H. A. Pan, J. F.Lee and N. L. Wu, *J. Power Sources*, 2014, **253**, 373.
56 M. A. Lowe, J. Gao and H. D. Abruña, *J. Mater. Chem. A*, 2013, **1**, 2094.
57 M. Pourbaix, "Altas of electrochemical equilibria in aqueous solutions," (2nd English ed.), National Association of Corrosion Engineers, Houston, TX, U.S.A. 1974.